Coupled discrete-continuum approach for railway ballast track and subgrade macro-meso analysis

Shi, Can; Zhao, Chunfa; Zhang, Xu; Guo, Yunlong

DOI
10.1080/10298436.2020.1721498

Publication date
2020

Document Version
Accepted author manuscript

Published in
International Journal of Pavement Engineering

Coupled Discrete-Continuum Approach for Railway Ballast Track and Subgrade Macro-meso Analysis

Can Shi[1], Chunfa Zhao[2]*, Xu Zhang[3], Yunlong Guo[4]

1. Ph.D. Candidate, State Key Laboratory of Traction Power, Southwest Jiaotong University, Chengdu 610031, China
2. Professor, State Key Laboratory of Traction Power, Southwest Jiaotong University, Chengdu 610031, China
3. Ph.D., School of Civil and Transportation Engineering, Guangdong University of Technology, Guangzhou, Guangdong 510006, China
4. Ph.D. Candidate, Faculty of Civil Engineering and Geosciences, Delft University of Technology, Delft, 2628CN, Netherlands

* Corresponding author, E-mail addresses: cfzhao@swjtu.edu.cn

Abstract: This paper presents a multi-layer railway ballast track and substructure model, where a coupled discrete and continuous method is used for macro-meso dynamic behaviour analysis under moving wheel loads. In this coupled model, the discrete element method (DEM) is utilized to build the superstructure of the ballast track (i.e. rail, fastener, sleeper and ballast layer), which considers the complex ballast shape and particle size distribution from mesoscopic level. The finite difference method (FDM) is used to simulate the substructure (i.e., subgrade and foundation) with a consideration of computing cost. And then, the coupled model is achieved by satisfying displacement, velocity and contact force compatibility between the FLAC and the PFC. Finally, the dynamic analysis is carried out by applying the wheel-rail forces obtained from a vehicle-track dynamics model into the coupled model. The DEM parameters of ballast particles are calibrated based on the results of the ballast direct shear tests, and the dynamic behaviour of railway ballast track and subgrade system is validated with the field measurement. Through the numerical analysis, it is confirmed that the coupled DEM/FDM model can reliably reflect macro-meso dynamic behaviour and accurately reveal the contact characteristics between the ballast layer and subgrade.

Keywords: Railway ballast track; Subgrade; Discrete element method; Finite difference method; Coupled model; Field test.

1. Introduction

Railway ballast track is the most traditional and universally preferred railway track structure because of its low construction cost and simplicity of maintenance. The structure is designed to withstand the imposed wheel loads, lower the railway operating costs, and keep passenger safety and comfort during the service life. In general, the

railway ballast track can be divided into two parts, namely the track superstructure and substructure. The track superstructure consists of fundamental elements, such as rails, fastening systems (elastic-pad and clamps), sleepers, and the substructure contains ballast layer, subgrade and foundation.

To study the dynamic behaviour of railway ballast track, a variety of theoretical and numerical methods have been proposed in the literature including different mathematical models (e.g. Zhai et al 2009; Adam et al. 2010; Giannakos 2010; Xu et al. 2017, 2018), finite element method (e.g. Hall 2003; Kuo and Huang 2009; Yang et al. 2009; Sayeed and Shahin 2016) and finite elements-boundary elements method (e.g. Takemiya et al. 1994; Adam et al. 2000; O'Brien and Rizos 2005; Galvín et al. 2010). However, these methods simplify the ballast layer as a spring-damping mass block. Therefore, it cannot reflect the discrete nature of the ballast layer from mesoscopic level (particle shape and size).

Deeper understanding of the railway ballast track dynamic behaviour requires an integration of field test and theoretical analysis. Hence the laboratory and field tests have been performed to reveal behaviour of railway ballast by Lackenby et al. 2007; Ataei et al. 2014; Qian et al. 2017; Guo et al. 2018; Zhang et al. 2019 a. These studies mainly concern the ballast assemblies and the dynamic behaviour of ballast particles under the train loads. However, the dynamic behaviour of railway ballast track and subgrade system has not been fully investigated.

To get through this limitation, the DEM has been recently applied in numerous studies on exploring the characteristics of ballast, which can provide a deeper insight into the mesoscopic ballast behaviour. The principle of the DEM, which is not based on macroscopic continuity hypothesis, is to discretize the research object into a set of discontinuous rigid elements. Recent studies clearly demonstrate that the DEM has been found to be the most promising tool to simulate ballast practice behaviour (e.g. Huang and Tutumluer, 2011; Qian et al. 2013; Ngo et al. 2016; Guo et al. 2019 a; Zhang et al. 2019 b). In these studies, the DEM has provided a deeper insight into the individual particle movements and interactions within the ballast assemblies.

Furthermore, based on the DEM, the dynamic behaviour of railway ballast track is also investigated by some scholars (e.g. Lobo-Guerrero and Vallejo 2006; Chen and McDowell 2016; Zhang et al. 2017; Ji et al. 2017). However, these studies mainly focused on the dynamic behaviour of ballast track without considering the subgrade elastic support, which may cause the inaccurate adjustment of ballast particles under the train loads. Additionally, Zhang et al. (2016) established a two-dimensional ballast track model utilizing the DEM with the concrete sleeper, clustered ballast stones and the silty clay subgrade, and analyzed the dynamic behaviour of track components under irregular vibration levels caused by train passing through the track. Ngo et al. (2016) proposed a

two-dimensional numerical model based on a coupled DEM and FDM to study the load-deformation response of the ballast assembly by considering the interaction between the ballast particles and the subgrade. Shao et al. (2017) established a three-dimensional combined discrete-finite element model to analyze the dynamic behaviour of railway ballast track under cyclic loads. However, the macro-meso dynamic behaviour of railway ballast track and subgrade cannot be fully investigated with these cross-sectional railway track models.

In this paper, a longitudinal railway ballast track and substructure model with coupled the DEM and FDM is built to analyze the dynamic behaviour of ballast track and subgrade and the interaction between them. In this coupled model, the ballast layer, sleeper, fastener and rail are built with the DEM. The continuous subgrade and foundation are built with the FDM, due to the numerical inability of the DEM to accurately model a large geometrical substructure, which contains an extremely large number of fine-grained soil particles. And then, the DEM and FDM are coupled by online displacement-force exchange. Afterwards, the dynamic wheel-rail forces obtained from a vehicle-track dynamics model (VTDM) are applied into the coupled model, and the macro-meso dynamic behaviour of railway ballast track and subgrade system is obtained. Finally, the laboratory and field tests are performed to validate this coupled model, and the correctness of the coupled model is verified by comparing the numerical results with experimental data.

2. Description of the proposed numerical model

The two-dimensional railway ballast track and substructure system is shown in Figure 1. The rail, fastener, sleeper and ballast layer are built through commercial DEM software called Particle Flow Code (PFC), and the subgrade and foundation layers are built through FDM software called Fast Lagrangian Analysis of Continua (FLAC). The interactions between the ballast layer and subgrade are facilitated by a series of interface elements generated between the PFC and FLAC boundary, and the coupling is achieved by exchanging the displacements, velocities and contact forces between two domains.

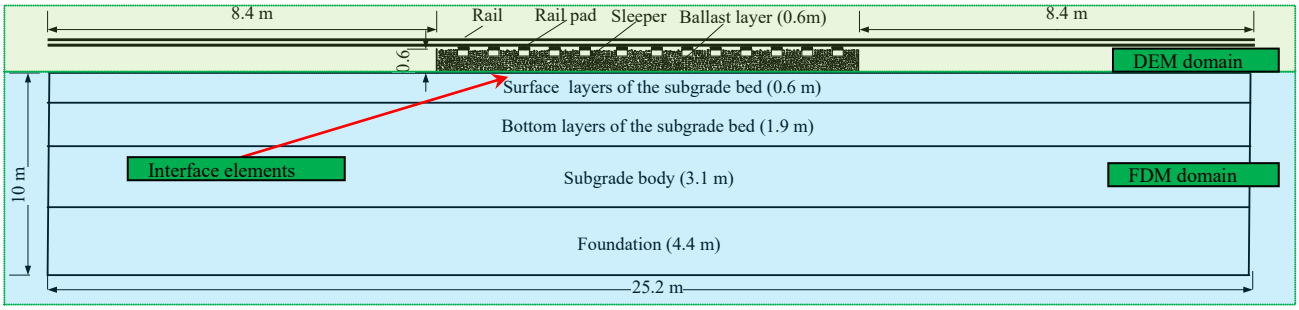

Fig. 1 Longitudinal railway ballast track and substructure profiles

In this coupled model, a railway ballast track with a length of 8.4 m (13 sleepers) is built in the DEM with the

distance of 60 cm between two adjacent sleepers, and the distance between the sleepers and the vertical boundaries is 60 cm. The length of rail and substructure is set to 25.2 m to reduce the influence of boundary constraints. The thickness of every layer in the coupled model is determined according to the Chinese Shuo-Huang heavy haul railway line, which is 0.6 m for the ballast layer, 0.6 m for the surface layer of subgrade, 1.9 m for the bottom layer of subgrade, 3.1 m for the subgrade body, and 5 m for the foundation.

2.1. DEM Model of railway ballast track

2.1.1. Ballast layer modelling

The railway ballast layer is constructed by well-graded crushed stones with irregular shapes, and the ballast shape has proven to be critical to the strength and stability of ballast aggregates (Lu and McDowell 2007). Studies on image analysis methods for granular materials have been reviewed by Guo et al. (2019 b). Even though it is easy and efficient to utilize sphere or disk unit to model ballast particles in PFC, the simple units like these cannot represent the interlocking between the ballast particles. In this work, the ballast particles with complex shapes are modelled by imaging-aided DEM approach. The complex shape of ballast particle, which is obtained by the image processing technology and hexagonal arrangement (one particle surrounded by other six particles) as shown in Figure 2, is considered in this paper.

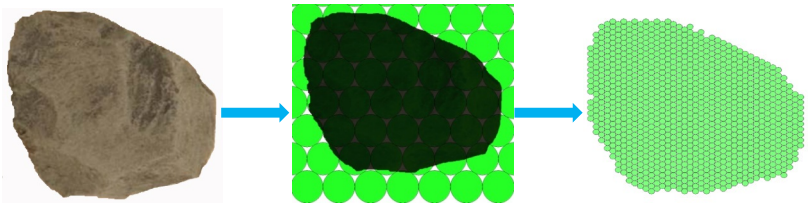

Fig. 2 Simulation of the ballast with complex shape

The creation process of a specific ballast particle shape is given as follow: (1) the digital camera is used to take photographs of the ballast particles; (2) a MATLAB programming code is used to convert the ballast photo into the binary image based on the image processing technology, and the profile curves of ballast particles are extracted from the binary images; (3) disk elements are generated to fill in the area enclosed by the real profile curve of a certain ballast particle; (4) the disk units are bonded together by large bond strength as a Cluster. Finally, a ballast sample library reflecting ballast particle shape is built. The ballast sample model can catch real irregular shapes of ballast samples quite well when the radius of the disk unit is small enough. Obviously, the smaller the radius of the disk unit is, the more accurate of the ballast particle will be. However, the computational efficiency will be significantly lowered due to the increase of the disk unit number. After calibration, the radius of disk unit is set to be 4 mm by taking both the model accuracy and the computational efficiency into account.

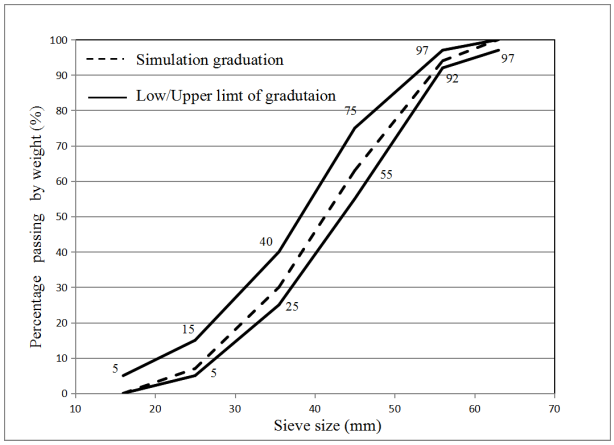

Fig. 3 Particle size distribution of the ballast materials

Furthermore, the existing studies are also concluded that the particle size distribution deeply influences performance of ballast assemblies (Bian et al. 2016). For this, based on the created ballast sample library (image-processing technology), the particle size distribution is also considered in this work. Firstly, the created ballast particles are classified according to the sieving size, and converted the mass percentage to the two-dimensional area percentage. Then, ballast particles are selected from the ballast sample library according to the passing area percentage. As shown in Figure 3, the selected particle size distribution lays in the middle of the Chinese existing heavy haul railway ballast gradation curves, which means it meets the particle size distribution requirement.

Table 1. Main DEM model parameter values of ballast particle

Parameters	Value	Unit
Ballast particle density	2600	kg/m^3
Ballast particle normal/shear contact stiffness	3×10^8	N/m
Ballast particle normal/shear bond strength	1×10^{10}	N
Ballast particle radius	4	mm
Ballast disk thickness	1.3	m
Ballast particle friction coefficient	0.7	—
Ballast viscous damping	0.05	—
Vertical wall normal/shear contact stiffness	3×10^8	N/m

In the DEM, the physical and mechanical behaviour of granular materials is determined by the contact constitutive relationship between particles. Herein, the linear contact model and the slip model (Itasca Consulting Group, Inc. 2004) are used to calculate the interaction forces between the ballast particles. Table 1 shows the main DEM model parameter values of the ballast particle. The disk unit density is set to 2600 kg/m^3, which is obtained according to the final ballast layer density (around 1800 kg/m^3). The normal and shear contact stiffness between ballast particles and the vertical walls are set to be the same value as the contact stiffness between ballast particles.

Friction is considered for all boundary walls, and the friction coefficient is the same as that between ballast particles.

2.1.2. Sleeper, fastener and rail modelling

PFC can not only simulates the discrete characteristics of ballast aggregate, but also simulate the continuous characteristics of the rail and sleeper through parallel bonding and clump (Itasca Consulting Group, Inc. 2004). In this work, the sleeper is simulated by combined 548 disk particles with the radius of 5 mm together as a clump (Super rigid element) based on the cross-section of type III concrete sleeper (as shown in Figure 7). According to the sleeper weight (350 kg) and the area of each disk, the disk particle density of 3129 kg/m^3 is obtained. The fastener is simulated by a disk particle with a radius of 20 mm laid on the sleeper, and the density of the fastener particles is set to 3184 kg/m^3 (according to the fastener weighs about 4 kg). And then the sleeper and fastener particles are bonded together without considering the sleeper and fastening system damage.

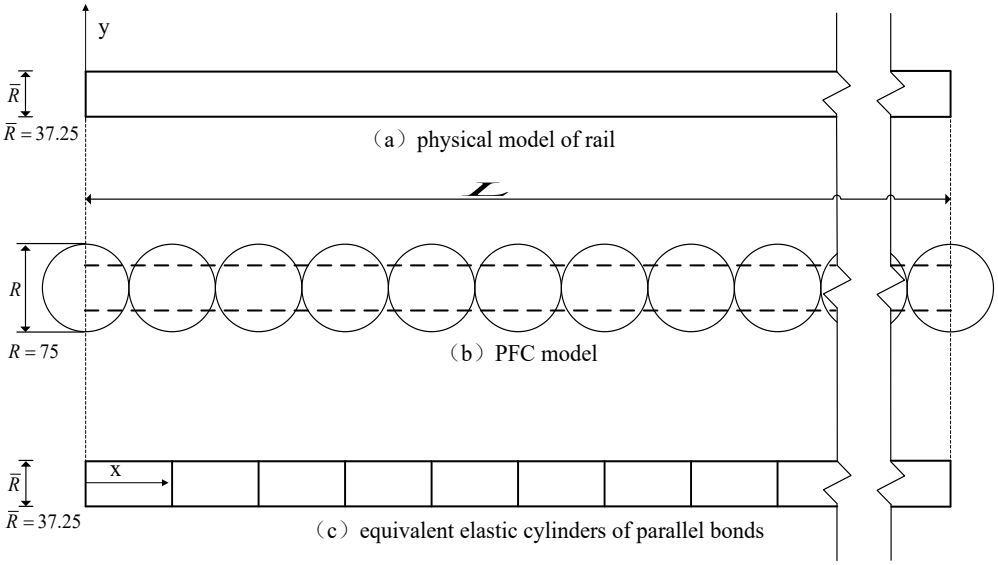

Fig. 4 Simulation of the rail in PFC

The rail is simplified as an equivalent beam with a rectangular cross-section, and its physical model is shown in Figure 4(a). The rail is modelled by combining a row of 169 disks with equal radius of 75 mm using parallel bonds, as shown in Figure 4(b). Figure 4(c) shows the equivalent elastic cylinders of parallel bonds. The parallel bonds can be assumed as a set of uniform springs in the contact plane, which is capable of transferring bending moments. The detailed description can be in referred to related work, such as (Itasca Consulting Group, Inc. 2004). The physical properties of a type 75 kg/m rail are given in Table 2. According to the rail properties, the mass of every 0.15 m (the length of each disk) is 11.25 kg, thus each rail disk particle has a density of 490 kg/m^3.

Table 2. Physical properties of the 75 kg/m rail

Length L/m	Cross-section area A/cm^2	Moment of inertia I/cm^4	Young's modulus E/Gpa	Density ρ/(kg/m^3)	Shear modulus G/Gpa	Poisson's ratio μ
25.2	95.037	4489	214	7800	82.946	0.29

A parallel bond is defined by the following five parameters: normal and shear stiffness ($\bar{k}^n$ and $\bar{k}^s$); normal and shear strength ($\bar{\sigma}_c$ and $\bar{\tau}_c$); and bond disk radius ($\bar{R}$). The normal and shear stiffness of the parallel bonds are chosen such that the collection of equivalent elastic cylinders, shown in Figure 4(c), mimics the physical rail. Thus, the chosen values are:

$$\bar{k}^n = \frac{E}{\bar{L}} = \frac{2.14\times10^{11}}{0.075\times2} = 1.427\times10^{12}(N/m^3) \tag{1}$$

$$\bar{k}^s = \frac{G}{\bar{L}} = \frac{8.2945\times10^{10}}{0.075\times2} = 5.5297\times10^{11}(N/m^3) \tag{2}$$

where $\bar{L}$ is the diameter of the rail particle.

The normal and shear strengths of the parallel bonds are set to be a large value (1×10^{10} N), such that bending moments arising from a sudden application of the wheel loads do not break the parallel bonds. The inertia moment of the rail model matches the real inertia moment of the cross section under the condition that the radius of parallel bond is obtained by Equation (1).

$$I = \frac{1}{12}t(2\bar{R})^3 \tag{3}$$

where I is the inertia moment of rail, t is the thickness of the rail disk particle, $\bar{R}$ is the radius of parallel bond, $\bar{R}$ = 37.25 mm in this study.

In the case all of the rail disk particles are set to the same stiffness, the equivalent stiffness of the entire beam (modeled using *n* parallel bonds and *n* contacts) can be express by

$$K = \frac{A\bar{k}^n}{n} + \frac{k^n}{2n} \tag{4}$$

where k^n is the normal stiffness of each ball, $A = 2\bar{R}t$ is the cross-sectional area of parallel bonds. Note that the contact stiffness for two balls with identical stiffness is equal to half the ball stiffness.

Therefore, the normal and shear stiffness of each of the balls (2.765×10^{11} N/m) are obtained by setting the second term of Eq. (4) equal to the overall beam stiffness of $AE/\bar{L}$.

The rail disk particles and the fastener particles are bonded by the bond strengths of 1×10^{10} N to make sure that the wheel/rail contact forces can be effectively transmitted to the other track components. The contact stiffness

of the sleeper is the same as that of the ballast particles, and the contact stiffness for the fastener particle is 120 kN/mm. Summarily, the DEM parameters of the rail disk particles are shown in Table 3.

Table 3. The discrete element parameters of rail, sleeper and fastener

Parameters	Value	Unit
Sleeper particle density	3129	kg/m^3
Sleeper particle radius	5	mm
Sleeper particle normal/shear contact stiffness	3×10^8	N/m
Sleeper particle normal/shear bond strength	1×10^{10}	N
Sleeper particle friction coefficient	0.7	—
Fastener particle density	3184	kg/m^3
Fastener particle radius	20	mm
Fastener particle normal/shear contact stiffness	1.2×10^8	N/m
Rail particle density	490	kg/m^3
Rail particle radius	75	mm
Rail particle parallel bond radius multiplier	0.497	—
Rail particle parallel bond contact normal stiffness	1.427×10^{12}	N/m^3
Rail particle parallel bond contact shear stiffness	5.5297×10^{11}	N/m^3
Rail particle parallel bond strength normal/shear	1×10^{10}	N
Rail particle normal/shear contact stiffness	2.765×10^{11}	N/m

The load-deformation behaviour of the PFC rail model is confirmed with a simply numerical test. As shown in Figure 5, the rail is simulated using parallel bonds as described previously, and the sleeper support is simulated by PFC wall elements. Then, a load *P* of 100 kN is applied at the middle point of the rail disk particles, with the un-balance forces of the walls are measured. Form Figure 5, it can be seen that the distribution of wheel load *P* mainly affects the adjacent 7 sleepers. The sleeper support forces (from left to right) are 0.029 *P*, 0.108 *P*, 0.236 *P*, 0.324 *P*, 0.236 *P*, 0.108 *P*, 0.029 *P*, which consist with the field test results, i.e. 0.02 *P*, 0.09 *P*, 0.22 *P*, 0.34 *P*, 0.22 *P*, 0.09 *P*, 0.02 *P* (Liu et al. 2015).

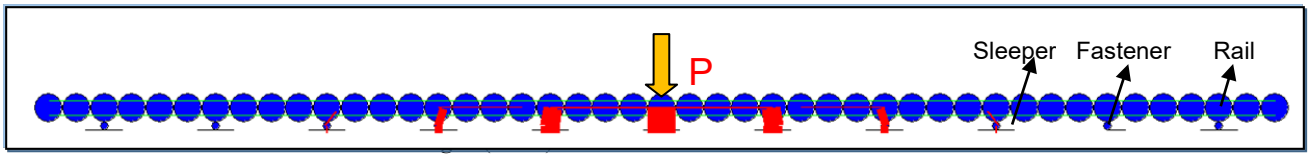

Figure 6 shows the initial state of the railway ballast track of the PFC model, and contact forces are presented at the contacts by red lines oriented in the direction of the forces. The thickness of the red line is proportional to its intensity, which can also be observed in Figure 5. As shown in Figure 6, obvious force chain structures can be seen in the ballast layer, and the contact forces of the crib ballast (ballast between sleepers) are rather small. The initial state of the railway ballast track indicates that the ballast layer is adequately compacted, where no stress concentration phenomenon is observed.

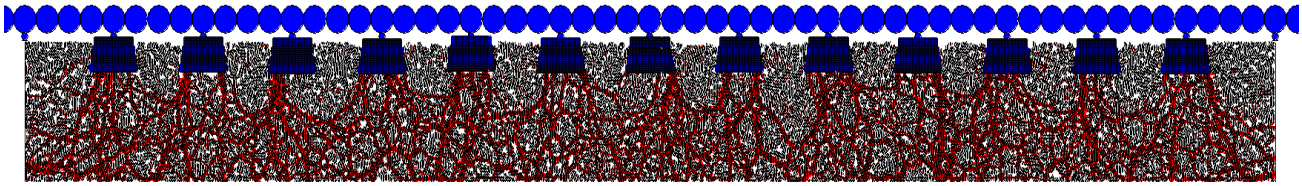

Fig. 6 (Color) The initial state of railway ballast track discrete element model

2.2. FDM model of subgrade and foundation

Because the computational cost is huge when the DEM is used to precisely simulate the subgrade and foundation, which contain lots of fine-grained soil particles. Therefore, the subgrade and foundation are treated as a continuous medium, and they are simulated with the finite difference software FLAC. The FLAC is an explicit finite-difference program for engineering mechanics computation with the continuum hypothesis. Based on the dynamic equations and dynamic method, the coordinates update with the solution of the time step integral. This continuum-based method is widely used to simulate the dynamic response, material yield and large deformation of the soil problem.

2.2.1. FDM model mesh

The mesh size of the subgrade is generally estimated by the smallest wavelength allowing the high-frequency motion to be simulated correctly. According to the studies conducted by Kuhlemeyer and Lysmer (1973), the mesh of the FDM model should be confirmed by the shortest wavelength of the input wave. Specifically, the mesh size must be less than 1/10-1/8 of the shortest wavelength. The propagation velocity of wave in substructure is calculated by

$$v_s = \sqrt{\frac{E}{2\rho(1+\mu)}} = \sqrt{\frac{G}{\rho}} \approx 100m/s \tag{5}$$

where λ is the wavelength, f is the frequency of the stress wave, E is the elastic modulus, G is the shear modulus, μ is the Poisson's ratio and ρ is the density.

The maximum concerned frequency of the substructure is usually no more than 100 Hz. Therefore, the effective wave length can be obtained by

$$\lambda = v_s / f = 1m \tag{6}$$

For the accurate description of wave propagation in soil materials and avoiding the numeric dispersion of the results, the mesh size should follow the equation:

$$\Delta l \le (\frac{1}{8} \sim \frac{1}{10})\lambda \tag{7}$$

where Δl is the distance between consecutive nodes.

Thus, a mesh size of 0.1 m × 0.1 m is adopted for the subgrade model. The FDM model size is 26 m × 10 m

including the subgrade and foundation, and the FDM model comprises a total of 52461 nodes and 52000 meshes.

2.2.2. Material parameters

The subgrade system is composed of three parts: the surface layers of subgrade bed, the bottom layers of subgrade bed and the subgrade body, as shown in Figure 1. This study focuses on the track dynamic response rather than on the long-term behaviour. Therefore, a classical isotropic and linear-elastic constitutive model is adopted for the three-layer subgrade system. The physical parameters of three-layer subgrade materials are shown in Table 4.

Table 4. Physical parameters of three-layer subgrade system

Track components	Poisson's ratio	Young modulus (MPa)	Density (kg/m^3)	Thickness (m)
Surface layer of subgrade bed	0.25	180	1950	0.6
Bottom layer of subgrade bed	0.25	110	1900	1.9
Subgrade body	0.3	80	1800	3.1

As shown in Table 4, all the subgrade layers are modelled with a constant Young modulus for each layer. However, in practice there is a consolidation for granular materials under pressure and the pressure is increasing with depth of the soil layer (Biarez and Hicher, 1994). Thus, the foundation layer is modelled using the following gradient law for elastic modulus:

$$E = E_0(\frac{P}{P_0})^n \tag{8}$$

where E_0 is a fitting parameter to adjust the Young modulus for a given value of a certain depth, herein, the target Young modulus value is 60 MPa at the foundation surface; P_0 is considered to be equal to the atmospheric pressure. The exponent n depends on the soil type. For clays it will be higher, between 0.7 and 0.9 (Biarez and Hicher, 1994), thus, it is set to 0.8 in this work. More detailed information for this choice can be found in the following paper (Arlaud et al. 2016).

2.2.3. Boundary condition and damping

To reduce the effects of boundary reflections, the viscous-spring artificial boundary (Liu and Li, 2005) is applied to the bottom of the foundation, which is equivalent to a distribution of spring-damper system in parallel. The spring constant K_B and the damping coefficient C_B can be expressed as follows:

$$K_{BN} = \alpha_N \frac{G}{R}, \quad C_{BN} = \rho c_p \tag{9}$$

$$K_{BT} = \alpha_T \frac{G}{R}, \quad C_{BT} = \rho c_s \tag{10}$$

where K_{BN} and K_{BT} are the spring normal and tangential stiffness coefficients; C_{BN} and C_{BT} are the spring normal and tangential damping coefficients; ρ is the mass density; G is the shear modulus; R is the distance between the wave source and the artificial boundary; c_p and c_s are the P-wave velocity and S-wave velocity

respectively； α_N and α_T denote the normal and tangent parameter respectively.

To propagate and dissipate the energy, the Rayleigh damping is adopted and set the same for all materials. The Rayleigh damping is expressed in matrix form and assumed to be proportional to the mass and stiffness matrices:

$$C = \alpha M + \beta K \tag{11}$$

where C is the damping matrix, M is the mass matrix, K is the stiffness matrix, α is the mass-proportional damping constant. β is the stiffness-proportional damping constant. The damping constant is given by:

$$\alpha = \xi_{\min} \omega_{\min} \tag{12}$$

$$\beta = \xi_{\min} / \omega_{\min} \tag{13}$$

where $\omega_{\min} = 2\pi f_{\min}$, $f_{\min}$ represents the central position of the approximate frequency independent span (i.e. central frequency), and $\xi_{\min}$ is the value of the critical damping ratio for this frequency.

The critical damping ratio range of the soil material is around 2 % to 5 %, and the critical damping ratio of 3 % is used. The value of $f_{\min}$ is chosen according to the literature (Itasca Consulting Group, Inc. 2005). The velocity at grid point without damping is recorded. Afterwards, the Fast Fourier Transform analysis is performed on the velocity records in order to confirm the dominant frequencies. In this case, the adopted dominant frequency is approximate to 11 Hz.

2.3. Framework of the coupled model

As mentioned above, the railway ballast track is built with the PFC software, and the subgrade and foundation system are modelled with the FLAC software. Since both of them are developed by the Itasca, they have a parallel configuration (I/O socket). The versions of FLAC 7.0 and PFC 3.0 are adopted in this work, which can use the socket I/O function to exchange data. And the coupling simulation is achieved (through the inserted FISH language) by exchanging displacements, velocities, and contact forces between the FLAC domain and the PFC domain. The coupling algorithm can be found in the software manual (Itasca Consulting Group, Inc. 2005) and the reference (Ngo et al. 2016). Figure 7 shows the coupled railway ballast track and infrastructure model. The x-axis is the longitudinal direction and the y-axis is the vertical direction. It should be pointed out that the longitudinal part of the model is not fully displayed. Several constraints are considered to ensure that the coupling process works properly. For example, the large-strain mode must be used in the FLAC model, and the time step in both softwares must be identical.

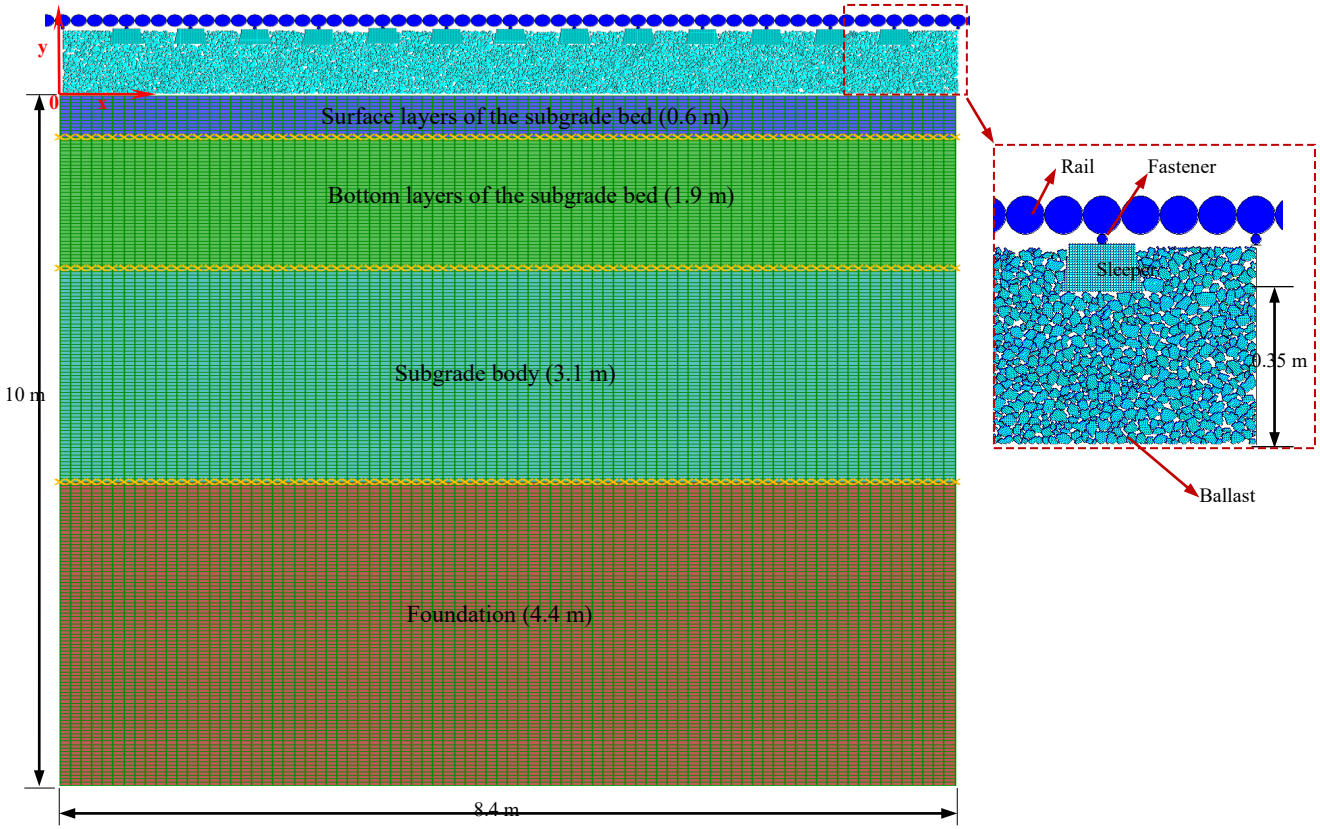

Fig. 7 Coupled railway ballast track and infrastructure model

A series of interface elements (PFC wall) are created between the PFC and FLAC to help implement the coupling process, and the force-displacement law is applied to derive the contact force acting on the boundary of the DEM and the FDM. The normal and tangential contact stiffness of the interface wall element is set to 1×10^{8} N/m by taking the effect of soft subgrade into account. The time step is set to 5×10^{-7} s for both the PFC and the FLAC. The procedures of the coupling process are described as follows:

(1) The railway ballast track is built in the PFC, and the subgrade and foundation system is built in the FLAC.

(2) Open the socket I/O function, the boundary nodal velocities in the FLAC (server) are written to an array along with the updated coordinates, and the data is sent to the PFC (client) through the socket connections.

(3) The PFC receives the data and uses the coordinates and velocities to update the interface wall coordinates. Then, the contact forces at the interface elements are obtained according to the force-displacement law.

(3) The contact forces are converted to the nodal forces, and applied to the elements of FLAC boundary.

(4) The coupled PFC and FLAC model starts next time step, and return to the second step.

A flowchart of the coupling process of the combined DEM-FDM model is illustrated in Figure 8.

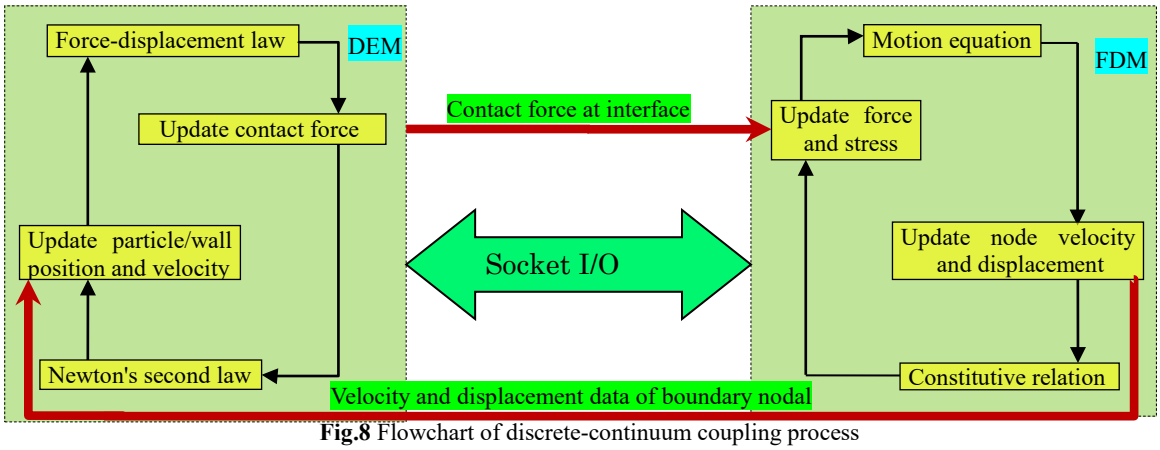

Fig.8 Flowchart of discrete-continuum coupling process

2.4. External excitation of the coupled model

When a railway vehicle traverses the railway track, it induces wheel-rail forces and track vibration. Here, a theoretical model of vehicle-track dynamics is established, and the wheel-rail forces are calculated based on the VTDM model (Zhai and Sun, 1994). In the VTDM model, the vehicle is regarded as a multi-rigid-body system. The rail is simulated as a Bernoulli-Euler beam separately supported by sleepers. Other track components are modelled as layers of springs and dampers or mass blocks. The nonlinear Hertz contact theory is adopted to calculate vertical wheel-rail forces. The details of this theory can be found in (Zhai et al. 2009), and the main parameters of the vehicle and the tracks are given in Appendix A. The VTDM model can accurately get the dynamic response of the vehicle-track interaction. A large number of practical engineering studies also demonstrate that the dynamic responses of the track system (wheel-rail forces, the rail and sleeper vibration) agree well with the field test results (Zhai et al. 2004). Hence, the wheel-rail forces calculated from the heavy haul VTDM model are applied to the proposed model as the external excitation.

The vehicle system and railway track are coupled through interaction forces between the wheels and the rails, where the track irregularity is the key factor affecting wheel-rail forces. Herein, the measured Shuo-Huang track irregularity (superimposed the short wavelength of 0.04 m) is used for the VTDM model. And the wheel-rail forces (as shown in Figure 9) are obtained when the HXD_1 locomotive with an axle load of 25 t run on the track at a speed of 80 km/h. From Figure 9, it can be seen that the wheel-rail forces fluctuate significantly around the static wheel load (125 kN) and the maximum value is around 180 kN. The symbols P_1, P_2, P_3, and P_4 represent the vertical wheel-rail forces of the first, second, third, and fourth wheelsets of a vehicle, respectively.

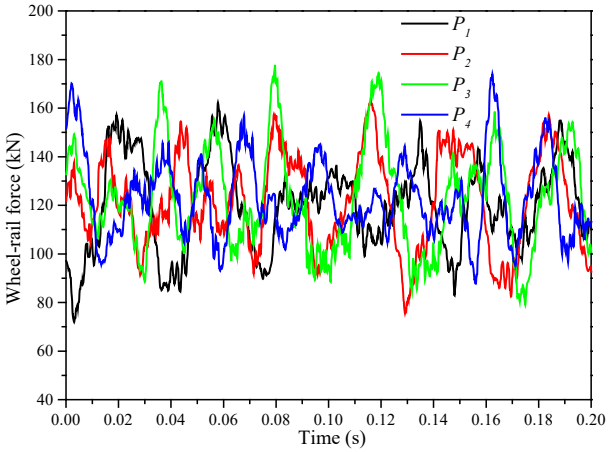

Fig. 9 (Color) Wheel-rail force curves of four wheelsets

Figure 10 demonstrates the four dynamic wheel-rail forces as inputs into the discrete-continuum model to simulate the dynamic action of a moving vehicle on the track. The four dynamic wheel-rail forces calculated by VTDM model are applied to the rail particles with a fixed distance, depending on the train speed and axle configuration. For instance, as the HXD_1 locomotive is adopted for the VTDM model, the distance between P_1 and P_2 (P_3 and P_4,) is kept as 2.8 m and the distance between P_2 and P_3 is kept as 6.2 m. At each time step, the forces are applied at different locations of the rail disk particles, and the wheel-rail forces are distributed linearly between the adjacent two rail disk particles according to its position when the loads are moving between the rail particles.

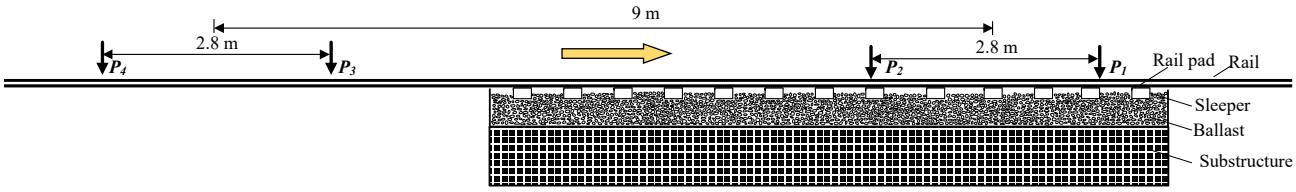

Fig. 10 Schematic of wheel-rail forces applied into the coupled DEM/FDM model

3. Numerical model verification and analysis

In order to validate this coupled model and get a deeper understanding of ballast aggregates and the railway ballast track, both laboratory and field tests are performed. Firstly, the DEM parameters of ballast particles are calibrated based on the direct shear tests results of the ballast assembly. Furthermore, the field test is carried out on the Shuo-Huang heavy haul line in China, and the dynamic response of the track components is obtained to verify the coupled model.

3.1. DEM ballast assembly parameter verification

3.1.1. Description of direct shear laboratory tests

To calibrate the proper parameters for the DEM ballast assembly, the macro performance from direct shear tests is utilized. The large-scale direct shear laboratory tests are performed under four different normal stresses at 20 kPa,

50 kPa, 100 kPa and 150 kPa, respectively. The large-scale direct shear apparatus consists of a lower box (size: 400 x 400 x 200 mm) and an upper box at the same size (as depicted in Figure 11). The apparatus control and the test data collection are managed through an automated data acquisition system. Normal stress is applied via a rigid and free plate placed on the top of the shear box using a servo hydraulic actuator.

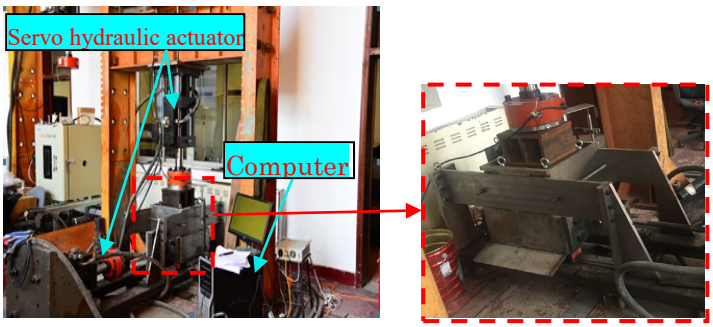

Fig. 11 Direct shear test: middle-scale direct shear apparatus with upper and lower shear boxes

The ballast used in the laboratory test is obtained from nearby ballast quarry, and involved ballast particles are at the range of 0.1 mm to 63 mm. After carefully sieving, the ballast particles are separated into four ranges of size by conducting sieve test (Figure 12 (a), (b)), and the ballast particles are mixed together to meet the particle size distribution (as shown in Figure 3). The ballast sample is packed and compacted in the shear box by cyclic harmonic normal load (Figure 12 (c)). During the shearing tests, the consistent normal stress is provided by the vertical servo hydraulic actuator, and the lower shear box is pushed horizontally by a horizontal hydraulic actuator at a speed rate of 2 mm/minute to a maximum horizontal displacement of 80 mm (10% strain) while the upper box remains stationary. The shear forces and the associated lateral displacements of the lower shear box are measured.

Fig. 12 Overview of the shear test preparation: (a) screening ballast; (b) classifying ballast; (c) loading ballast

3.1.2. Direct shear test simulations and verification

According to laboratory test conditions, a series of direct shear test simulations are carried out under different normal stresses. Figure 13 shows the DEM direct shear box test model with irregular shaped particles, and the previously mentioned ballast layer modelling processes are applied to simulate ballast assemblies. In this direct shear model, a total of 143 Cluster ballast particles are generated at random orientations considering the gradation, and the ballast particles are compacted to a density of 1850 kg/m^3 to resemble experimental conditions. The

breakage of ballast is not considered during shearing. The applied normal stress remains constant by adjusting the position and velocity of the top plate using the numerical servo control mechanism (Itasca Consulting Group, Inc. 2004), and the stress is computed by taking average wall forces divided by appropriate areas. Similar to laboratory conditions (four normal stresses), the lower shear box is pushed to move horizontally at a velocity of 0.5 mm per time step (the time step used in numerical simulation is 1 x 10^{-6} per second) while the upper part is fixed.

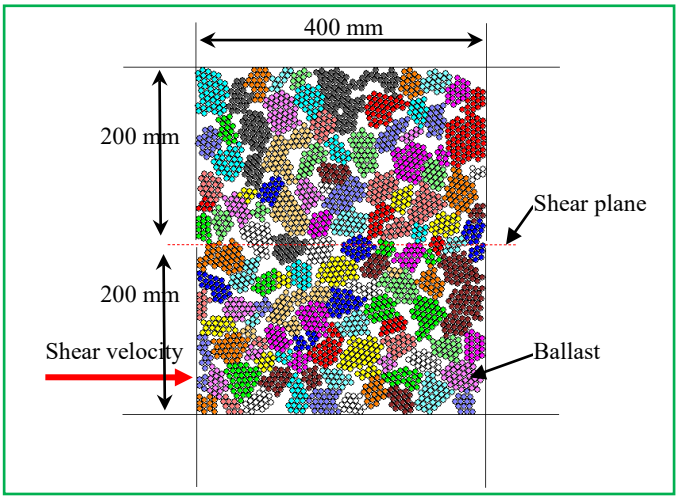

Fig. 13 (Color) Initial assembly of large-scale direct shear test

Figure 14 presents comparisons of the shear stress-strain results of ballast assembly obtained in the laboratory with those measured from the DEM simulations. The experiment and simulation results show that the peak shear stress increases with an increase of the normal stresses, which is consistent with earlier studies conducted by Indraratna et al. 2012; Estaire and Santans 2018. The DEM simulation results show a noticeable discrepancy in stress-strain curves with markedly decreased stress compared with the laboratory data. It is mainly because the two-dimensional DEM model only considers the shapes of ballast in a plane, thus the random distribution of ballasts in the direction of perpendicular to the plane cannot be considered. This results in a large stress fluctuation in the shearing process. From Figure 14, the shear stress simulation results are somewhat higher when compared with the experimental results, which mainly due to the 2D model limits the movement and interaction of ballast aggregates in one plane and cannot take the contact forces between ballast aggregates in three dimensions into account. Moreover, the difference may be attributed to the abrasion and fracture of ballast particles that could not be accurately captured in the DEM analysis. In general, the DEM simulation results match reasonably well with the laboratory data under the applied normal stresses. Based on these discussions, it is reasonable to conclude that the proposed DEM parameters are capable of capturing the shear stress-strain behaviour of ballast assembles.

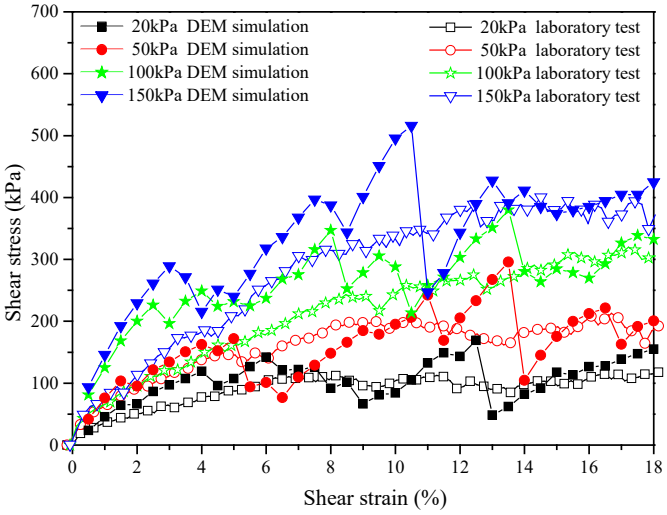

Fig. 14 The shear stress-strain results

3.2. Coupled model verification and analysis

After applying the above wheel-rail forces (as described in section 2.4) into the coupled DEM/FDM model, the simulation results of dynamic behaviour of the railway ballast track and subgrade system can be obtained. A field measurement is performed on Shuo-Huang heavy haul line, and the dynamic wheel-rail forces, the accelerations of track components, vertical displacements of sleepers are measured when a freight train passes through the test site at a speed of 80 km/h. And then, a validation of the coupled model is carried out by comparing the field measured results with simulation results. Afterward, the meso analysis of railway ballast track is carried out to better understand the mechanical behaviour of the track infrastructure during moving loads.

3.2.1. Description of the field test

In order to verify the validity of the coupled model, a field test is carried out on the Chinese Shuo-Huang heavy haul line, whilst mechanical properties of the ballast layer are also explored. In the field test, the railway line utilizes a continuously welded 75 kg/m rail, with type II fastening and type III concrete sleepers at a spacing of 0.6 m. The ballast layer is approximately 0.6 m deep. The subgrade is constructed according to Chinese railway standards (National Railway Administration of P.R. China, 2005). It consists of three distinct layers, the upper of which is a 0.6 m layer of stiff sand gravel, the middle layer consists is 1.9 m made up of at least 50% gravel, sand and silts, and the bottom layer is made of medium strength sand silt and is approximately 3.1 m deep. Figure 15(a) shows a freight train passing the field test sites. The monitoring procedure includes measurements of the rail-wheel forces, the acceleration of rail, sleeper and ballast. The sleeper displacement is measured relative to the subgrade surface as the ballast layer deform.

Fig. 15 Field testing: (a) field test location; (b) displacement sensors; (c) accelerometer on rail; (d) accelerometer on sleeper; (e) accelerometer embedded in ballast layer; (f) data acquisition system

Various types of instruments are used to obtain the track responses: (1) rail shear deformations are measured using the strain gauges to assess wheel-rail forces (Figure 15(b)); (2) the sleeper displacement is measured using the linear variable displacement transducer sensor (Figure 15(b)); (3) vertical accelerations of sleeper and rail are measured using piezoelectric accelerometer (Figure 15(c) and 15(d)); (4) ballast acceleration are measured using the embedded accelerometers in the ballast layer under the sleeper at 0.15 m and 0.3 m depth (Figure 15(e)), and a special box with the same weight as ballast is used to avoid the damage of accelerometer according to Refers. (Zhai et al, 2004). Meanwhile, Figure 15(f) shows the data acquisition system. In this case study, an acquisition frequency of 5000 Hz is measured for these acceleration sensors. The acquisition frequency of 1000 Hz is adopted for other types of sensors. Because of the random nature of the dynamic response for high frequencies due to track and wheel irregularities and contact collision between ballasts (which are outside the scope of this study), low-pass filters are applied for an easier interpretation of the results. The low-pass filters with frequencies of 500 Hz and 300 Hz are respectively applied to the acceleration time history records of the sleeper and ballast.

Measurements are performed as a freight train passes through the test site at a speed of 80 km/h, and the dynamic response of the track components is obtained to verify the discrete-continuous coupled model. The locomotive of HXD_1 is approximately 35 m long and consisted of two identical 4-axle locomotives connected by internal reconnection links. The wheel base of the bogie is 2.8 m, the longitudinal distance between the two bogie centers is 9 m and the axle load is 250 kN. An example of the dynamic wheel-rail force measurement is presented in Figure 16. The maximum field test value induced by the locomotive is in the range of 140.2 kN ~ 180.3 kN, which is also close to the peak amplitude of wheel-rail forces calculated from the VTCD. As this locomotive is

consisted of two identical 4-axle locomotives, the dynamic response of track components induced by the two bogies of the front locomotive is used to calibrate this coupled discrete-continuum model.

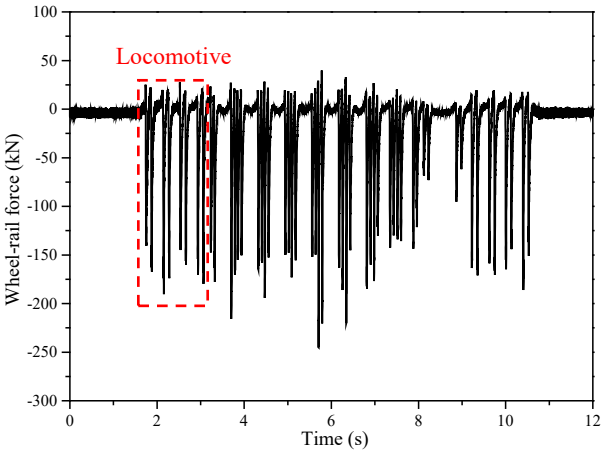

Fig. 16 The measured wheel-rail force

3.2.2. *Dynamic behaviour of railway ballast track*

Figure 17 shows the simulation results of the rail bending moment. The rail bending moment includes the maximum positive bending moments (M^{+}_{max}) and the maximum reverse bending moments (M^{-}_{max}). From Figure 18, it can be seen that M^{+}_{max} occurs beneath the wheelsets and M^{-}_{max} occurs between the wheelsets. The value of M^{+}_{max} is about 32 kN•m, which is very close to the measured value (Nielsen and Oscarsson, 2004). And the value of M^{-}_{max} (10 kN•m) is close to the empirical data (Fallah Nafari et al, 2018). The sleeper displacement results (related to the subgrade surface) compared with the measured results are shown in Figure 18. It can be observed that the maximum sleeper displacement is about 1.2 mm and the numerical result is close to it.

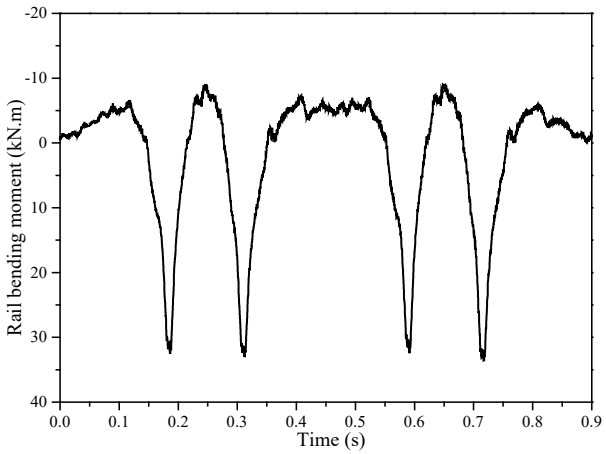

Fig. 17 Simulation results of rail bending moment

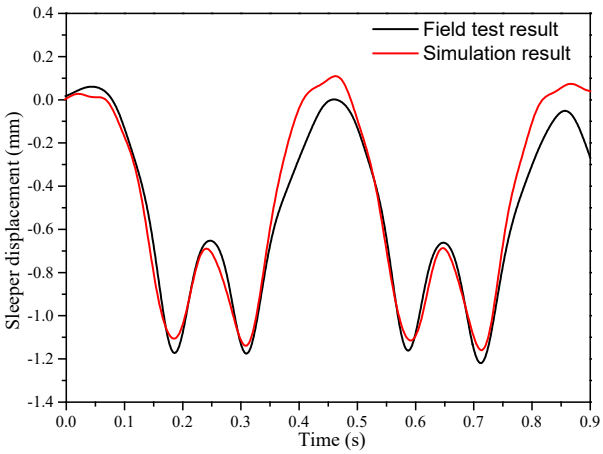

Fig. 18 (Color) Sleeper displacement results

Figure 19-20 present the comparison between numerical and field test acceleration results of the rail and sleeper. In general, track vibration caused by the passing of four wheelsets can be identified, and the waveform of the simulation results agrees well with the field test results. As illustrated in Figure 19, the maximum rail

acceleration of the field test result is 10 g, and the simulation result is 15 g. The numerical result of rail acceleration has relatively higher negative peaks, which may result from the constraint conditions at the rail ends. Figure 20 shows that the numerical results are in good agreement with the field test results and both of the maximum sleeper accelerations are about 2.1 g.

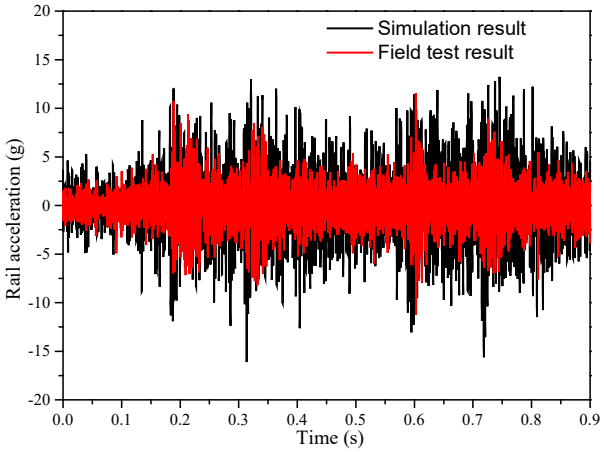

Fig. 19 (Color) Rail acceleration results

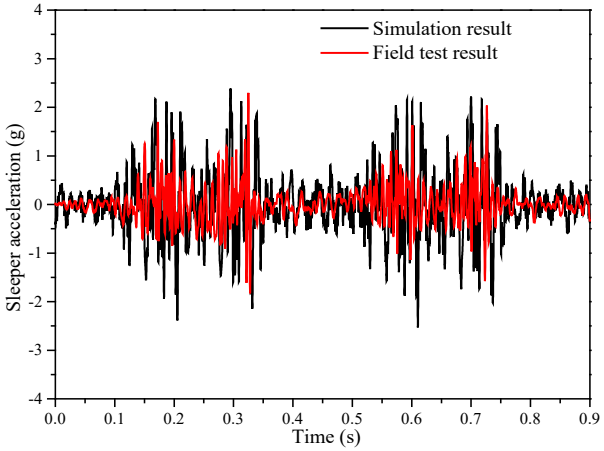

Fig. 20 (Color) Sleeper acceleration results

Figure 21 presents the results of ballast accelerations at two depths (0.15 m and 0.30 m under the sleeper, similar to the ballast positions tested in the field). The acceleration of ballast at 0.15 m under the sleeper is larger than that of ballast at 0.3 m under the sleeper. It can be seen that the peak accelerations of the numerical results are higher than the field test results. This difference may be caused by the outline shape of the special box used to measure the ballast acceleration, which is different from the actual ballast, and the two-dimensional coupled model, which only allows the ballast to move in a plane and contact force between ballast particles cannot be dispersed by other particles in the direction of perpendicular to the plane. Through comparison and analysis, it can be observed that the waveform and amplitude of simulation results are also close to the field test results. Therefore, the coupled model of DEM domain is validated.

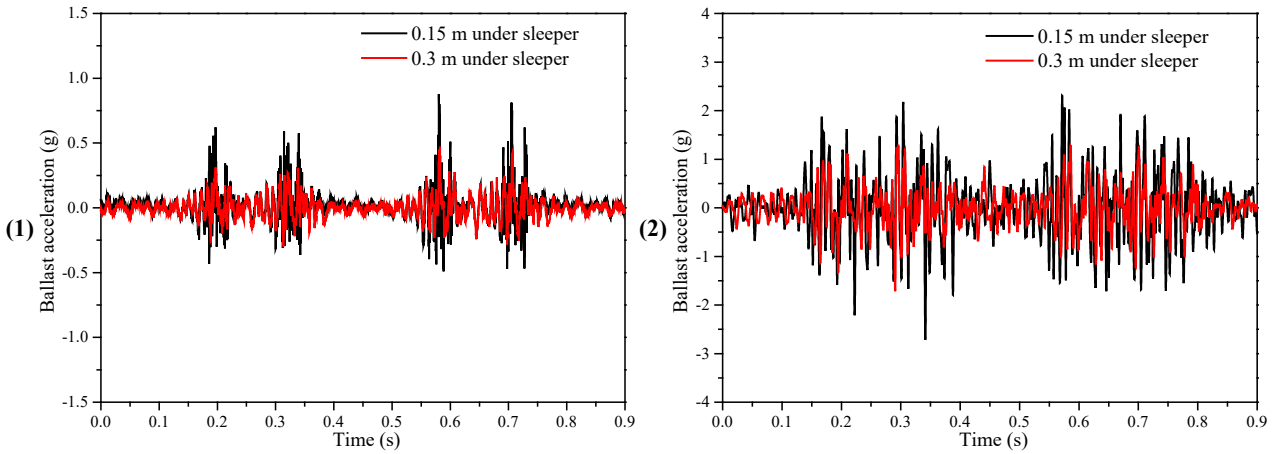

Fig. 21 (Color) Ballast acceleration results: (1) field test result; (2) simulation result

3.2.3. Dynamic behaviour of subgrade system

To further verify the reliability of this coupled model, the numerical results (stress and acceleration) of the subgrade surface are compared with these of the field test. The subgrade stress and acceleration are two important parameters used for estimating the effects of vibration on the subgrade failure. Figure 22-23 show the dynamic behaviour of subgrade surface stress and acceleration under the sleeper in the middle of the model. It is observed that the peak stress on the subgrade surface is 61.8 kPa, and the peak acceleration of the subgrade surface is 6 m/s^2. According to the field measurement carried out at the Shuo-Huang railway line under the conditions of various freight trains passing, the dynamic stress on the subgrade surface ranges from 50-100 kPa (Mei et al. 2019; Bian et al. 2014). The subgrade acceleration measured from the field ranges from 2 m/s^2 to 6 m/s^2, based on the results in Cui et al. 2014 and Chebli et al. 2008. In summary, the dynamic behaviours of both the railway ballast track and subgrade system agree well with the test results, so the effectiveness and reliability of the coupled model are verified.

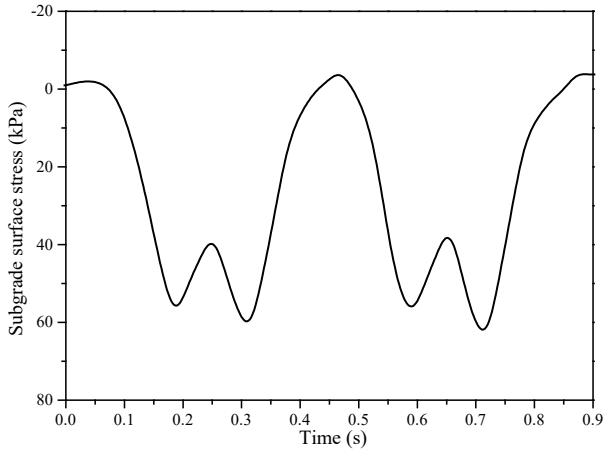

Fig. 22 Simulation results of subgrade dynamic stress

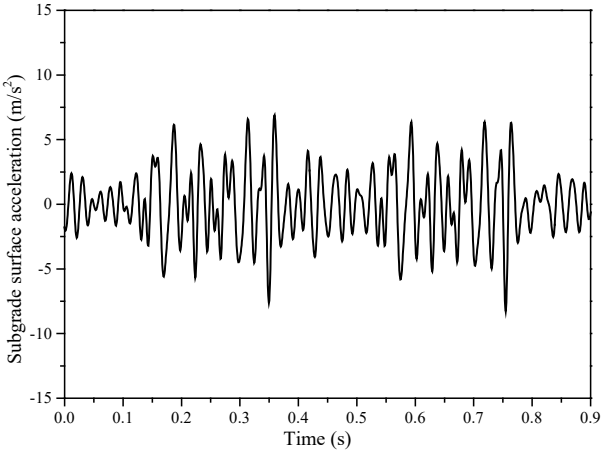

Fig. 23 Simulation results of subgrade dynamic acceleration

Figure 24 shows the maximum dynamic stress on the subgrade surface along the track during the passage of the locomotive with an axle load of 25 t. It can be obtained that the stress at both ends of subgrade surface is obviously smaller, which is mainly influenced by the boundary conditions of the proposed model. Meanwhile, the stochastic characteristics can be observed for the maximum dynamic stresses on the subgrade surface along the track, and the mean of the subgrade surface stress values is 61.5 kPa from x = 1 m to x = 7.4 m. The maximum dynamic stresses are randomly distributed along the track, which is mainly affected by the complex contact state between ballast particles and subgrade.

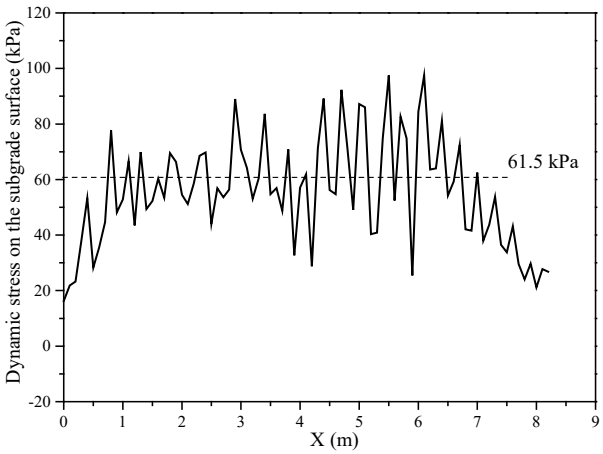

Fig. 24 Longitudinal distribution of the maximum dynamic stresses on the subgrade surface

3.3. Meso-mechanical analysis of ballast track

3.3.1. Spatial distribution of contact force and vertical yy-stress

Figure 25 presents the contact force chain of ballast layer together with vertical yy-stress contour of substructure when the first wheelset arrives at different positions. The symbols P_1 and P_2 express the dynamic loads of the first and second wheelset, respectively (same in Figure 9). Figure 25 shows that the moving loads cause the contact forces between the wheelsets larger than other areas and the yy-stress decreases with the increase of the depth from the subgrade surface. Small stress bulbs are formed on the subgrade surface under the moving loads, this means that certain areas on subgrade surface is closely contacted with ballast particles and bear large stress, while others are subject to small loads. The uneven distribution of stress on the subgrade surface is mainly influenced by the uneven compaction of the ballast layer. In addition, as the forward movement of the wheelsets, the regions with large contact force and yy-stress move forward. However, the force chain structure in ballast layer and the positions of small stress bulbs remain unchanged, but the size and color of stress bulbs changes due to the influence of wheel-rail forces. This implies that the force chain structure of ballast layer is fairly stable and the regions where subgrade surface closely contact with the ballast particles are more susceptible to damage.

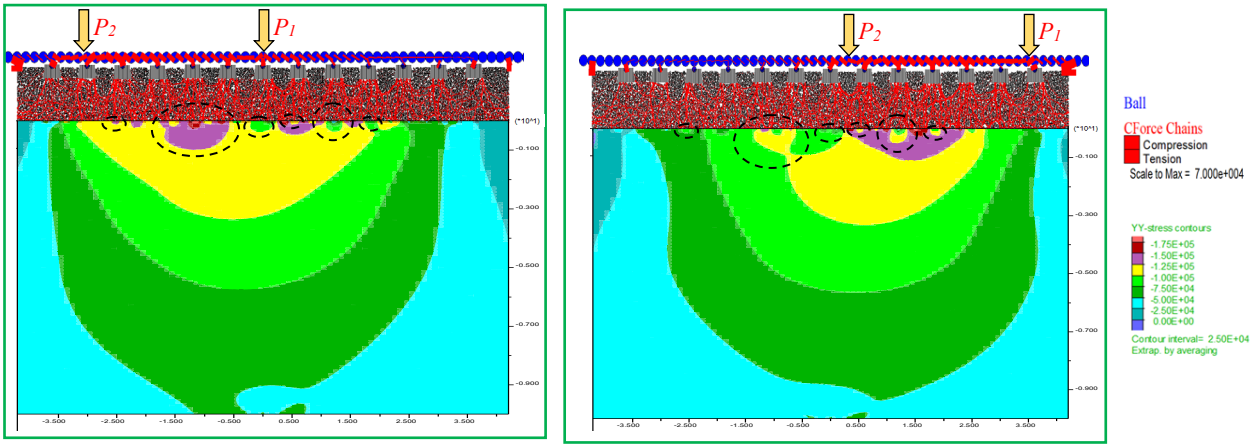

Fig. 25 (Color) The change of vertical stress contour σ_{yy} and contact force under moving loads

3.3.2. Spatial distribution of track infrastructure movements

Figure 26 demonstrates the displacement vector plots of the ballast aggregates and substructure soils when the first wheelset arrives at different positions. Similarly, it can be found that the area of large displacement vector moves forward with the forward movement of the wheelsets. Observing two graphs when the wheelset arrives at different positions, the region with largest displacement vector of the ballast aggregates appears in an indefinite region between the two wheelsets, rather than in the region below the wheelsets. This indicates the ballast aggregates in this area is relatively loose and the track of this area is more likely to undergo permanent deformation. Meanwhile, it can be seen that the bogie with a 2.8 m wheelbase influences the length of ballast layer displacement vector is 4.2 m and the depth of the subgrade is 2.8 m.

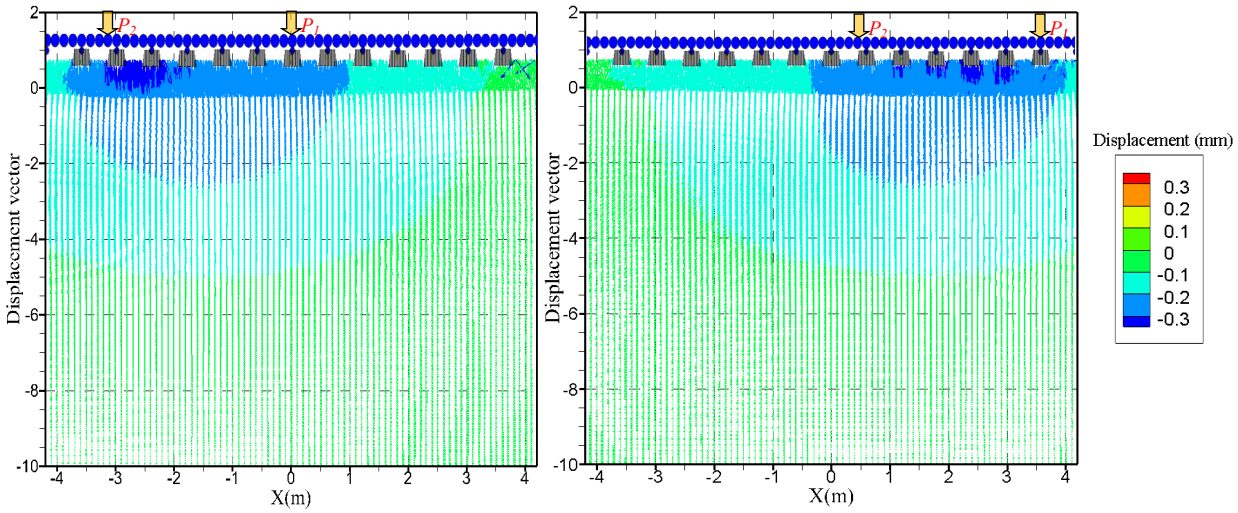

Fig. 26 (Color) The change of the displacement vector graph under moving loads

Figure 27 demonstrates the acceleration vector plots of the ballast aggregates and substructure soils when the first wheelset arrives at different positions. Figure 27 shows that the spatial distribution of acceleration vector of ballast aggregates and subgrade soils are irregular, which is mainly caused by the complicated interaction between ballast particles. In addition, the acceleration vectors ballast aggregates in the areas near the wheelsets are significantly larger than other areas. As described in Figure 27, the acceleration vectors of ballast aggregates near the first wheelset shows more upward movement trend, while the response near the second wheelset generally has a tendency to move downward. This implies that the phenomenon of ballast flying is more likely to occur at the front of the vehicle.

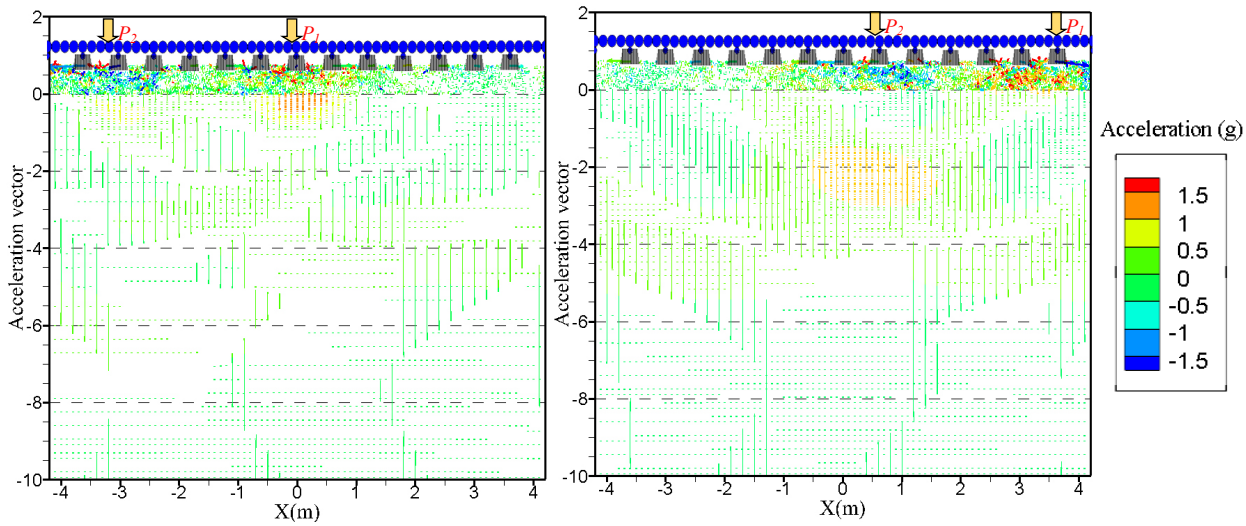

Fig. 27 (Color) The change of the acceleration vector graph under moving loads

4. Conclusions

A coupled model combining both finite and discrete elements is proposed in this work, which can be used to analyze the meso-mechanical and macro-mechanical behaviour of railway ballast track and subgrade system. In this coupled model, the ballast layer, which consists of realistic shapes of discrete crushed stones, is modelled with the implemented imaging aided DEM approach. The rail is modelled as a beam with parallel bonds by bonding the particles together, and the sleepers are modelled as a rigid body. Afterwards, three layers of the subgrade system and the foundation are modelled with the FDM as a continuous medium. Finally, the integrated railway ballast track and substructure system is built with exchanging displacements, velocities, and contact forces between the two softwares. This coupled model can not only overcome the computing cost limitations, but also take advantages of the capabilities of the two methodologies.

In order to validate this coupled model and comprehensively investigate the dynamic responses of railway track infrastructure, the laboratory and field tests are performed. The direct shear tests of ballast aggregates are performed to calibrate the ballast particles parameters in the DEM. Furthermore, the field test is carried out on the Shuo-Huang heavy haul line in China, and the dynamic response of the track components is measured when a freight train passes through the test site at a speed of 80 km/h. Moreover, the VTDM model with the same condition as the field test is established, and the vehicle-track interaction forces calculated from the VTDM model are applied to the rail disk particles of the coupled model. Subsequently, the numerical simulation results of the ballast track and subgrade system (vibration characteristics) are compared with the field test results. The results show that the dynamic behaviour (waveform and amplitude of track components) of the simulation results agree

well with field test results, this indicates the effectiveness and reliability of the coupled model.

As described above, the coupled DEM and FDM model can provide reliable results for the macro-mechanical ballast behaviour under the moving loads. In addition, this coupled model can provide a feasible approach to study the mesoscopic dynamic behaviour of railway ballast track and subgrade system, and can analyze the realistic interaction mechanism between ballast layer and subgrade. From mesoscopic behaviour analysis, the conclusions can be obtained that there is obvious stress inhomogeneity on the subgrade surface affected by the force chain of ballast layer and the phenomenon of ballast flying is more likely to occur at the front of the vehicle.

Furthermore, developing a reliable numerical model for accurate analysis of the track behaviour is the first step of predicting track geometry deformation, and the DEM demonstrates a realistic tool for track geometry deformation analysis. In this work, it is observed that some regions have obviously larger ballast displacement vectors than other regions, which replies the railway ballast track in this region is more prone to permanent deformation. Therefore, this coupled model provides an underlying approach to study track geometry deformation characteristics and deterioration behaviour of the railway infrastructure, which can potentially help to schedule ballast maintenance and rehabilitation activities.

Founding

This research is supported by National Natural Science Foundation of China [grant number 51578469 and U 1234209]; and State Key Laboratory of Traction Power [grant number 2015TPL-T12].

Reference

[1]. Zhai, W.M., Wang, K.Y., and Cai, C.B. (2009). Fundamentals of vehicle-track coupled dynamics. *Vehicle System Dynamic*, 47(11), 1349-1376.

[2]. Adam, D., Brandl, H., & Paulmichl, I. (2010). Dynamic aspects of rail tracks for high-speed railways. *International Journal of Pavement Engineering*, 11(4), 281-291.

[3]. Giannakos, K. (2010). Theoretical calculation of the track mass in the motion of unsprung masses in relation to track dynamic stiffness and damping. *International Journal of Pavement Engineering*, 11(4), 319-330.

[4]. Xu, L., Zhai, W., and Gao, J. (2017). A probabilistic model for track random irregularities in vehicle/track coupled dynamics. *Applied Mathematical Modelling*, 51, 145-158.

[5]. Xu, L., Chen, X., Li, X., and He, X. (2018). Development of a railway wagon-track interaction model: Case studies on excited tracks. *Mechanical Systems and Signal Processing*, 100, 877-898.

[6]. Hall, L. (2003). Simulations and analyses of train-induced ground vibrations in finite element models. *Soil Dynamics and Earthquake Engineering*, 23(5): 403-413.

[7]. Kuo, C.M., and Huang, C.H. (2009). Two approaches of finite-element modeling of ballasted railway track. *Journal of geotechnical and geoenvironmental engineering*, 135(3), 455-458.

[8]. Yang, L.A., Powrie, W., and Priest, J.A. (2009). Dynamic stress analysis of a ballasted railway track bed during train passage. *Journal of Geotechnical and Geoenvironmental Engineering*, 135(5), 680-689.

[9]. Sayeed, M.A., and Shahin, M.A. (2016). Three-dimensional numerical modelling of ballasted railway track

foundations for high-speed trains with special reference to critical speed. *Transportation Geotechnics*, 6, 55-65.

[10]. Takemiya, H., Fei, G., and Sukeyasu, Y. (1994). 2-D transient soil-surface foundation interaction and wave propagation by time domain BEM. *Earthquake Engineering & Structural Dynamics*, 23(9), 931-945.

[11]. Adam, M., Pflanz, G., and Schmid, G. (2000). Two- and three-dimensional modelling of half-space and train-track embankment under dynamic loading. *Soil Dynamics and Earthquake Engineering*, 19(8): 559-573.

[12]. O'Brien, J., and Rizos, D.C. (2005). A 3D BEM-FEM methodology for simulation of high speed train induced vibrations. *Soil Dynamics and Earthquake Engineering*, 25(4), 289-301.

[13]. Galvín, P., Romero, A., and Domínguez, J. (2010). Fully three-dimensional analysis of high-speed train-track-soil-structure dynamic interaction. *Journal of Sound and Vibration*, 329(24): 5147-5163.

[14]. Lackenby, J., Indraratna, B., McDowell, G., and Christie, D. (2007). Effect of confining pressure on ballast degradation and deformation under cyclic triaxial loading. *Géotechnique*, 57(6), 527-536.

[15]. Ataei, S., Mohammadzadeh, S., Jadidi, H., & Miri, A. (2014). Effects of maintenance operations on railway track's mechanical behaviour by field load testing. *International Journal of Pavement Engineering*, 15(3), 215-227.

[16]. Qian, Y., Boler, H., Moaveni, M., Tutumluer, E., Hashash, Y. M., and Ghaboussi, J. (2017). Degradation-related changes in ballast gradation and aggregate particle morphology. *Journal of Geotechnical and Geoenvironmental Engineering*, 143(8), 04017032.

[17]. Guo, Y., Markine, V., Song, J., and Jing, G. (2018). Ballast degradation: Effect of particle size and shape using Los Angeles Abrasion test and image analysis. *Construction and Building Materials*, 169, 414-424.

[18]. Zhang, X., Zhao, C., Zhai, W., Shi, C., and Feng, Y. (2019 a). Investigation of track settlement and ballast degradation in the high-speed railway using a full-scale laboratory test. *Proceedings of the Institution of Mechanical Engineers, Part F: Journal of Rail and Rapid Transit*, 233(8): 869-881.

[19]. Huang, H., and Tutumluer, E. (2011). Discrete element modeling for fouled railroad ballast. *Construction and Building Materials*, 25(8), 3306-3312.

[20]. Qian, Y., Lee, S., Tutumluer, E., Hashash, Y., Mishra, D., and Ghaboussi, J. (2013). Simulating ballast shear strength from large-scale triaxial tests: Discrete element method. *Transportation Research Record: Journal of the Transportation Research Board*, (2374), 126-135.

[21]. Ngo, N.T., Indraratna, B., and Rujikiatkamjorn, C. (2016). Micromechanics-based investigation of fouled ballast using large-scale triaxial tests and discrete element modeling. *Journal of Geotechnical and Geoenvironmental Engineering*, 143(2), 04016089.

[22]. Guo, Y., Markine, V., Qiang, W., Zhang, H., and Jing, G. (2019 a). Effects of crumb rubber size and percentage on degradation reduction of railway ballast. *Construction and Building Materials*, 212, 210-224.

[23]. Zhang X., Zhao C. & Zhai W. (2019 b). Importance of load frequency in applying cyclic loads to investigate ballast deformation under high-speed train loads. *Soil Dynamics and Earthquake Engineering*, 120:28-38.

[24]. Lobo-Guerrero, S., and Vallejo, L. E. (2006). Discrete element method analysis of railtrack ballast degradation during cyclic loading. *Granular Matter*, 8(3-4), 195.

[25]. Chen, C., and McDowell, G. R. (2016). An investigation of the dynamic behaviour of track transition zones using discrete element modelling. *Proceedings of the Institution of Mechanical Engineers, Part F: Journal of Rail and Rapid Transit*, 230(1), 117-128.

[26]. Zhang, X., Zhao, C.F., and Zhai, W.M. (2017). Dynamic behavior analysis of high-speed railway ballast under moving vehicle loads using discrete element method. *International Journal of Geomechanics*, 04016157.

[27]. Ji, S., Sun, S., and Yan, Y. (2017). Discrete element modeling of dynamic behaviors of railway ballast under cyclic loading with dilated polyhedral. *International Journal for Numerical & Analytical Methods in Geomechanics*, 41, 180-197.

[28]. Zhang, Z., Zhang, X., Qiu, H., and Daddow, M. (2016). Dynamic characteristics of track-ballast-silty clay with irregular vibration levels generated by high-speed train based on DEM. *Construction and Building Materials*, 125, 564-573.

[29]. Ngo, N.T., Indraratna, B. and Rujikiatkamjorn, C. (2016). Simulation ballasted track behavior: numerical treatment and field application. *International Journal of Geomechanics*, 04016130.

[30]. Shao, S., Yan, Y., and Ji, S. (2017). Combined discrete-finite element modeling of ballasted railway track under cyclic loading. *International Journal of Computational Methods*, 14(05), 1750047.

[31]. Lu, M., and Mcdwell, G.R. (2007). The importance of modelling ballast particle shape in the discrete element method. *Granular Matter*, 9(1), 69-80.

[32]. Guo, Y., Markine, V., Zhang, X., Qiang, W., and Jing, G. (2019 b). Image analysis for morphology, rheology and degradation study of railway ballast: A review. *Transportation Geotechnics*, 18,173-211.

[33]. Bian, X., Huang, H., Tutumluer, E., and Gao, Y. (2016). "Critical particle size" and ballast gradation studied by Discrete Element Modeling. *Transportation Geotechnics*, 6, 38-44.

[34]. Itasca Consulting Group, Inc. (2004). Particle Flow Code in 2 Dimensions, version 3.1, User's Mannual.

[35]. Liu, G., Luo, Q., Zhang, L., and Jiang, L. (2015). Analysis of the design load on the high-speed railway ballasted track subgrade. *Journal of Railway Science and Engineering*, 12(3), 475-481 (in Chinese).

[36]. Kuhlemeyer, R.L., and Lysmer, J. (1973). Finite element method accuracy for wave propagation problems. *Journal of Soil Mechanics & Foundations Div*, 99(Tech Rpt).

[37]. Biarez, J., and Hicher, P.I. (1994). Elementary mechanics of soil behaviour: Saturated remoulded soils. *A.A. Balkema*.

[38]. Arlaud, E., D'Aguiar, S. C., and Balmes, E. (2016). Receptance of railway tracks at low frequency: Numerical and experimental approaches. *Transportation Geotechnics*, 9, 1-16.

[39]. Liu J. and Li B. (2005). A unified viscous-spring artificial boundary for 3-D static and dynamic applications. Science in China Series E Engineering & Materials Science, 48(5): 570-584.

[40]. Itasca Consulting Group, Inc. (2005). Fast Language Analysis of Continua in 2 Dimensions, Version 5.0, *User's Mannual*.

[41]. Zhai, W.M., and Sun, X. (1994). A detailed model for investigating vertical interaction between railway vehicle and track. *Vehicle System Dynamic*, 23(suppl), 603-615.

[42]. Zhai, W.M., Wang, K.Y., and Lin, J.H. (2004). Modelling and experiment of railway ballast vibrations. *Journal of Sound Vibration*, 270(4-5), 673-683.

[43]. Indraratna, B., Ngo, N.T., Rujikiatkamjorn, C., and Vinod, J.S. (2012). Behavior of fresh and fouled railway ballast subjected to direct shear testing: discrete element simulation. *International Journal of Geomechanics*, 14(1), 34-44.

[44]. Estaire, J., and Santana, M. (2018). Large direct shear tests performed with fresh ballast. *In Railroad Ballast Testing and Properties*. ASTM International.

[45]. National Railway Administration of P.R. China. (2005). Design standards for railway embankments. TB10001- 2005, *China Railway Publishing*, Beijing (in Chinese).

[46]. Nielsen, J.C., and Oscarsson, J. (2004). Simulation of dynamic train-track interaction with state-dependent track properties. *Journal of sound and vibration*, 275(3-5), 515-532.

[47]. Fallah Nafari, S., Gül, M., Hendry, M. T. and Cheng, J. R. (2018). Estimation of vertical bending stress in rails using train-mounted vertical track deflection measurement systems. *Proceedings of the Institution of Mechanical Engineers, Part F: Journal of Rail and Rapid Transit*, 232(5), 1528-1538.

[48]. Mei, H., Leng, W., Nie, R., Liu, W., Chen, C., and Wu, X. (2019). Random distribution characteristics of peak dynamic stress on the subgrade surface of heavy-haul railways considering track irregularities. *Soil Dynamics and Earthquake Engineering*, 116, 205-214.

[49]. Bian, X., Jiang, H., Cheng, C., Chen, Y., Chen, R., and Jiang, J. (2014). Full-scale model testing on a ballastless high-speed railway under simulated train moving loads. *Soil Dynamics and Earthquake Engineering*, 66, 368-384.

[50]. Cui, Y. J., Lamas-Lopez, F., Trinh, V. N., Calon, N., D'aguiar, S. C., Dupla, J. C., ... and Robinet, A. (2014). Investigation of interlayer soil behaviour by field monitoring. *Transportation Geotechnics*, 1(3), 91-105.

[51]. Chebli, H., Clouteau, D. and Schmitt, L. (2008). Dynamic response of high-speed ballasted railway tracks: 3D periodic model and in situ measurements. *Soil Dynamics and Earthquake Engineering*, 28(2), 118-131.

Appendix

Table A1. Main parameters of railway vehicles used in the simulation

Parameter	unit	Value	Parameter	unit	Value
Car body mass	kg	61927	Vertical Stiffness coefficient of the primary suspension (each axis)	N/m	2.123×10^{6}
Bogie mass	kg	7840	Vertical stiffness coefficient of the secondary suspension	N/m	1.67×10^{6}
Wheelset mass	kg	5430	Damping coefficient of the primary suspension (each axis)	N/m	2.5×10^{4}
the car body nodding inertia	$kg\cdot m^2$	1.443×10^{6}	Damping coefficient of the secondary suspension	N/m	1.0×10^{5}
the bogie nodding inertia	$kg\cdot m^2$	1.311×10^{3}	Semi-longitudinal distance between bogies	m	4.5
Wheel radius	m	0.43	Semi-longitudinal distance between wheelsets in a bogie	m	1.4

Table A2. Main parameters of the railway tracks used in the simulation

Parameter	unit	Value	Parameter	unit	Value
Elastic modulus of the rail	Pa	2.14×10^{11}	Density of ballast	$kg\cdot m^{-3}$	1800
Inertia moment of rail cross section	m^4	3.217×10^{-5}	Elastic modulus of ballast	Pa	1.0×10^{8}
Mass of the rail	kg	74.414	Damping coefficient of ballast	$N\cdot s\cdot m^{-1}$	5.88×10^{4}
Mass of sleeper (half)	kg	175	Shear stiffness of ballast	$N\cdot m^{-1}$	5.0×10^{7}
Vertical stiffness of rail pad	$N\cdot m^{-1}$	1.2×10^{8}	Shear damping coefficient of ballast	$N\cdot s\cdot m^{-1}$	4×10^{4}
Damping coefficient of rail pad	$N\cdot s\cdot m^{-1}$	5×10^{4}	Thickness of ballast	m	0.6
Sleeper spacing	m	0.6	K_{30} modulus of subgrade	Pa	1.0×10^{8}